

# Instruments for particle size and settling velocity observations in sediment transport

Y.C. Agrawal\*, H.C. Pottsmith

*Sequoia Scientific, Inc., Westpark Technical Center, 15317 NE 90th Street, Redmond, WA 98052, USA*

Received 21 May 1999; accepted 20 March 2000

## Abstract

In this paper we describe two sensors for measurement of particle size-distribution and settling-velocity distribution. These measurements are critical to the correct estimation of the true sediment concentration in the field, as well as to evaluating models for transport rates of sediments. A multi-angle measurement of laser scattering is made and inverted to obtain the particle size distribution. Since small-angle scattering is relatively insensitive to particle composition, the size distribution measurements are robust, and do not require particle refractive index. It is shown that with a knowledge of the size distribution, true particulate volume concentration can be obtained, unaffected in calibration by changes in particle size distribution. The data from bottom boundary layer experiments using the instrument show the presence of temporal variability in size distribution associated with the strength of forcing of the boundary layer. The importance of these observations lies in the implication that historical data acquired with single-parameter optical or other sensors needs to be revisited. In the second instrument, analyzing the observation of size distributions during settling in a settling column produces settling velocity estimates. In this case, the history of concentration of each size class is examined to determine the settling velocity, without invoking any assumptions of settling regime. Settling velocity data from a field experiment off the New Jersey coast fit the model:  $w_{f,n} = 0.45 \times 10^{-3} a_n^{1.2}$ , where  $a_n$  is radius in microns and settling velocity is in cm/s. © 2000 Elsevier Science B.V. All rights reserved.

*Keywords:* Sediment transport; Settling velocity; Laser diffraction

## 1. Introduction

We introduce the present instruments by first describing the quantities needed for studies in sediment transport. This is followed by a survey of the state-of-the-art of instrumentation preceding this work. We then review the principles of laser diffraction that underlies the two instrument systems described in this paper. We present this description with sufficient rigor, such that a reader may discern

all steps in the process and follow the mathematical details. Subsequently, we describe the instruments, the laboratory verification and calibration procedures. Field data from each instrument is presented. The focus in this paper is on instrumentation, so that we leave a detailed description of scientific findings to subsequent papers.

For the sediment transport scientist, the governing equations relating sediment distribution to hydrodynamics are the combination of the boundary layer equations, and the equation for sediment mass conservation. When sediment concentrations are small, the equations for fluid motions and for particles

\* Corresponding author. Fax: +1-425-867-5506.

E-mail address: yogi@sequoiasci.com (Y.C. Agrawal).

de-couple. In this case, sediment distribution is described, in its simplest one-dimensional form by:

$$C_{n,t} + w_{f,n}C_{n,z} = [KC_{n,z}]_z \quad (1)$$

where  $C_n$  is the *volume concentration* of the  $n$ th size class,  $w_{f,n}$  is the fall velocity for the  $n$ th size class,  $K$  is eddy viscosity, and subscripts  $t$  and  $z$  denote differentiation with respect to time  $t$  and vertical coordinate  $z$ , respectively. Thus the first requirement for sediment observations is for the concentration by sizes  $C_n$ . The second is the *fall velocity* by sizes  $w_{f,n}$ . Model testing of Eq. (1) for the concentration distribution  $C_n(z)$  requires the eddy viscosity  $K$  and a bottom boundary condition for  $C_n(z)$ . The literature on solution of the hydrodynamics to solve for  $K$  is rich (e.g. the survey by Wiberg (1995)). The third quantity necessary to solve the equation is the bottom boundary condition, i.e.  $C_n$  at some reference height  $z_r$ . For this bottom boundary condition, a widely used formulation is based on the work of Smith (1977) which specifies the concentration of sediments at a reference height—the *reference concentration*. Due to the vast array of factors influencing sediment properties—sediment size distribution, biological cohesiveness, bedforms, wave-directional spread etc.—the specification of the ‘reference concentration’ remains one of the most intractable problems in sediment transport. Measurements provide an empirical, site-specific approach for advancement. This application requires the measurement of size specific concentration  $C_n$  at a small distance above the seafloor.

### 1.1. Prior sensors for sediments

In most cases, suspended sediment ‘concentration’ has been estimated via one parameter—optical transmission (Moody et al., 1987), optical backscatter (Downing et al., 1981), or acoustic scattering cross-section (Crawford and Hay, 1993; Lynch et al., 1994; Thorne and Hardcastle, 1997). These are all one-parameter sensors, where a single parameter represents the sediment concentration. A one-parameter sensor necessarily obtains a weighted sum of the concentrations of underlying size classes. For example, optical transmission or backscatter sensors estimate approximate (*not exact*) total particle cross-sectional area. In contrast, acoustic sensors, usually operating in the Rayleigh regime (i.e. when the insonifying acoustic

wavelength  $\lambda_a$  is of the same order or greater than the particle diameter, i.e.  $k_a a < 1$  where  $k_a = 2\pi/\lambda_a$ ) respond to the sum of the squares of particle volumes. For particles of 1 mm diameter or smaller, this condition is satisfied at acoustic frequencies of 1 MHz or lower. Thus, neither of these sensors simply sum the mass or volume concentrations to provide the needed measure of  $C_n$  or the total concentration  $\sum C_n$ . For this reason, unless the particle size distribution is invariant in space and time, the calibration of these single-parameter sensors in laboratories before field usage, while a common practice, is of limited value. An unfortunate consequence of the use of such calibrations is the absence of error bounds in the interpretation of data. It is likely that historical data with these unknown errors in estimating concentration are, in part, responsible for some of the large variability in predictive capability of sediment transport models. Regardless, the power of multi-frequency acoustics to provide range-gated sand concentration field is to be recognized as significant for nearshore sediment observations.

To estimate the multi-valued size-distribution  $C_n$ , a multi-parameter sensor must obviously be employed. Multi-frequency acoustics appear to offer attractive advantages, e.g. their line-of-sight, range-gated synoptic capability. However, probing a wide dynamic range of particle sizes requires a similarly large range of frequencies in a multi-frequency system. This constitutes a practical restriction in use. Hay and Sheng (1992) have used acoustic sizing with a 3-frequency system, assuming an underlying log-normal particle size distribution. They reported estimates of sand concentrations. The technique could not reach small sizes of order 10  $\mu\text{m}$  due to the requirement for frequencies well above 10 MHz to get sufficiently short acoustic wavelengths. Sound at the high frequencies necessary to achieve wavelengths of say 100  $\mu\text{m}$  (e.g. 15 MHz) attenuates very strongly in water, making range penetration severely limited. Thus there exists a mismatch between the size range of naturally *suspended* sediments and the ability to produce small acoustic wavelengths needed to measure these fine particles. Nonetheless, acoustics have contributed much to our knowledge of sediment distributions in boundary layers.

In contrast to the multi-frequency acoustic approach of Hay and Sheng (1992), optics afford a

capability to observe a wider range of particle sizes, although without the benefit of range-gated profiling. By measuring optical scattering over a wide dynamic range of *angles* (the dynamic range is defined here as the ratio of maximum to minimum scattering angle), a multi-parameter measurement is obtained with information content on a correspondingly large dynamic range in particle sizes. The angular dynamic range is typically 100:1 or 200:1 so that size ranges from, say, 1–200  $\mu\text{m}$  can be studied with a single instrument. This principle is called laser diffraction. The name derives from the approximation to the exact solution to Maxwell's equations describing light scattering by spheres. The exact solution for homogeneous spheres of arbitrary size, due to Mie, (Born and Wolf, 1975), has the property that for large particles, i.e. when the real part  $m$  of the complex refractive index, and particle size  $k_a$  ( $k$  being  $2\pi/\lambda$ ,  $\lambda$  is optical wavelength) are such that  $(m - 1)k_a \gg 1$ , the scattering at small forward angles appears nearly identical to the diffraction through an equal diameter aperture (Born and Wolf, 1975; Swithenbank et al., 1976). An even more significant observation is that under these conditions, as small angle scattering is dominated by diffraction, the light that passes through the particle does not affect the small angle measurement. However, only the light passing through the particle experiences the particle refractive index (i.e. composition); hence, the refractive index of particles becomes largely irrelevant. This implies that particle composition, or for that matter, *possibly* particle internal structure and homogeneity, are of little to no consequence. As the particle composition does not determine its scattering characteristics, the method is fully general for particle sizing. It is for this reason, that this has become the most widely used particle ensemble sizing method, employed for measuring diverse types of particles, including cements, chocolates or microbes.

The first underwater instrument based on laser diffraction was developed by Bale and Morris (1987). They adapted a commercial laboratory instrument manufactured by Malvern Instruments of UK for ocean use. They have presented results from estuarine particle sizing (Eisma et al., 1996). Recently, a team of French scientists has employed a submersible instrument manufactured by CILAS (Gentien et al., 1995). In both these cases, the precise mathematical

algorithm used to convert the observed angular scattering distribution to particle size distribution was not revealed. The present authors originally employed a different design. Multi-angle scattering was observed using a CCD line array photo-detector (Agrawal and Pottsmith, 1994). Whereas successful, the use of CCDs unnecessarily required long averaging times to remove the influence of laser speckle, and also required complex, fast electronics. For these reasons, in this work we have also migrated to the discrete circular ring detectors (see later) that are commonly used in commercial laboratory instruments. The instruments described in this paper, in contrast to those of Bale and Morris and Gentien et al. mentioned above, are autonomous, battery-powered, and are equipped with a computer and memory for data storage.

Of the two instruments that are the subject of this paper, the first instrument, LISST-100 (LISST is acronym from *Laser in-situ Scattering and Transmissometry*) obtains the size distribution on a programmable schedule up to a year, but is typically restricted to a shorter duration by bio-fouling of windows. The second instrument described here, LISST-ST, obtains the settling velocity for 8 size classes in the 5–500  $\mu\text{m}$  range.<sup>1</sup> Natural particles are known to exhibit settling velocities that are dependent not just on size but also on composition, which is generally poorly quantified. In the laboratory, siliceous particles have been studied commonly to evaluate the validity of Stokes' law. An exhaustive study of the settling velocity of particles in the laboratory was reported by Dietrich (1982). He offered a review of literature and synthesized the settling velocity data in dimensionless form. His work confirms the validity of Stokes settling at low Reynolds numbers, though when the particle shape departs significantly from spheres, as with fibers, the settling velocity formulation requires a correction factor. It can be shown that, according to Stokes law, the settling velocity in water,  $w_{f,n}$  (in cm/s) is related to particle size  $a_\mu$  (expressed in microns), and specific density  $s$  as:

$$w_{f,n} = 0.22 \times 10^{-3} (s - 1) a_\mu^2 \quad (2)$$

At Reynolds number  $R_e = 2aw_{f,n}/\nu$  in the vicinity of

<sup>1</sup> More recent instruments cover the range 1.2–250  $\mu\text{m}$ , or 2.5–500  $\mu\text{m}$ .

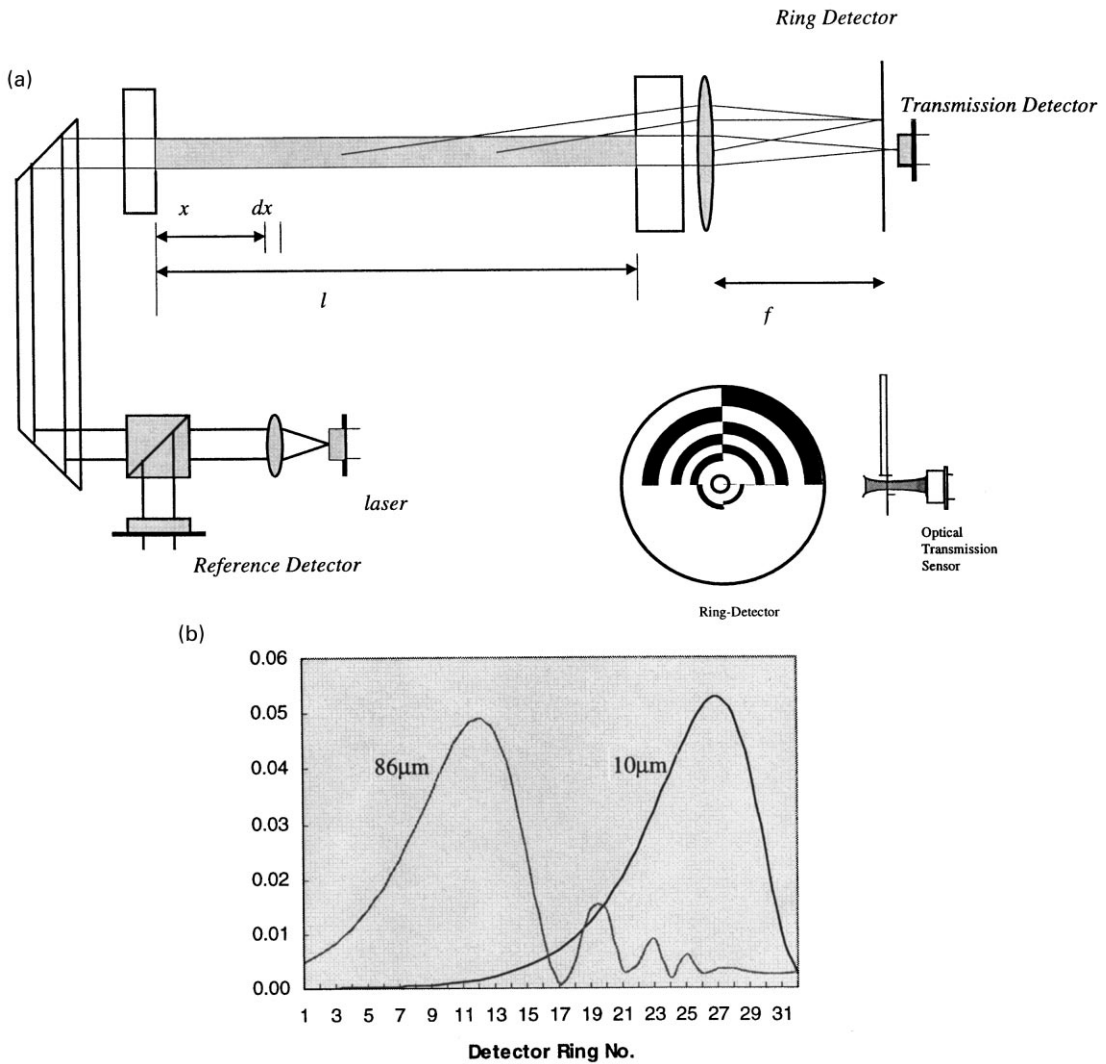


Fig. 1. (a) Basic optical geometry shows laser, optics and detectors. The details of the ring-detector are shown; the edge view of the ring detector shows the location of the photodiode behind the ring -detector. This photodiode senses the optical transmission. (b) Scattering signature of particle size: large sizes put their maximum scattering at small rings and vice versa.

1, based on fluid viscosity  $\nu$ , particle diameter  $2a$ , and fall velocity  $w_f$ , the fractional increase to the drag coefficient under Oseen flow is  $[3/16]R_e$ . At still higher Reynolds numbers additional drag on particles reduces the exponent still further, eventually reaching a value of 0.5 for fully turbulent flow (Dietrich, 1982).

Because much of the suspended material in water is expected to fall by Stokes' law, it is worth considering the consequence of particle sizes on vertical distribution of particles. For example, within the inertial

region of a boundary layer, a linear dependence of eddy viscosity on distance from the seafloor produces a vertical distribution, related to that at a reference height  $z_r$ , of the form:

$$C_n(z) = C_n(z_r)[z/z_r]^{-w_{r,n}/k u_*}$$

where  $k$  is the von Karman's constant ( $k = 0.41$ ) and  $u_*$  is the friction velocity, defined as usual, with stress  $\tau_w$  and water density  $\rho$  as:  $u_* = (\tau_w/\rho)^{1/2}$ . Since the

fall velocity for particles in the Stokes regime scales with the particle radius squared, it is seen that

$$C_n(z) \propto z^{-\beta a^2}; \quad \beta = 0.22 \times 10^{-3}(s - 1)/[\mathbf{k}u_*] \quad (3)$$

The square of particle radius in the exponent has these implications: First, the size distribution of suspended particles can be expected to be a strong function of particle diameter. This is borne out by experience, in that coarse sand hugs the bed and is transported principally as bedload, whereas fines are mixed relatively well and transport as suspended load. Second, when  $\beta a^2$  is of order one, from Eq. (2), the exponent of  $z$  in Eq. (3) can produce large errors in estimating concentrations from small errors in the knowledge of particle size. In energetic oceanic situations  $\mathbf{k}u_*$  is of order 1, so that size-related vertical variation may be strongest for siliceous particles of diameter near 30  $\mu\text{m}$  and above. In field observations to be presented in subsequent papers, we shall show clear evidence of this strong vertical gradient in concentrations of the larger particles.

A substantial scientific effort continues to be expended in the estimation of in-situ settling velocities of particles, especially of marine aggregates, (Fennessy et al., 1994; Jones and Jago, 1996; Puls and Kuhl, 1996; Van Leussen, 1996), and a comparison of the several research devices is presented by Dyer et al. (1996). Much of the work for measuring settling velocities is surveyed by Hill et al. (1994), who developed their own settling device Remote Optical Settling Tube, ROST. In the present work on measurement of settling velocities, the size is measured as the equivalent optical sphere. Thus, unlike all prior sensors, no assumption on particle density is necessary. For determining the settling velocity, particles are trapped in a settling column. As the particles of any size-class settle through the length of the settling column  $L$  and then disappear over time  $T_B$ , the concentration history of each size class is employed to estimate the settling velocity simply through  $w_{f,n} = L/T_B$ . In this manner, one obtains the settling velocity for as many size classes as can be resolved optically.

Among the capabilities of the instruments described in this paper is their ability to self event-trigger. Using the built-in pressure and temperature sensors, a data schedule can be programmed which

adapts to tides, surface waves, storms (using pressure or pressure variance) or fronts (temperature gradients). For example, in this paper, by high-pass filtering the pressure record with samples at 15 min intervals, we show estimates of surface gravity waves. Also, the measurement of optical transmission is included as a necessary auxiliary parameter for the size distribution measurement, so that these instruments add to the capabilities of the widely used optical transmissometer.

## 2. Laser diffraction principles

The signature of particle size is described in simple physical terms next. For the geometry of Fig. 1a, consider the scattering of collimated laser light by small particles as detected by a specially constructed detector. The detector is placed at the focal plane of a receiving lens of focal length  $f$ . All rays originating from a scatterer at a particular angle  $\theta$  to the lens optical axis reach a point on the focal plane at a radius  $r = f\theta$ . The radii of the detector rings increase logarithmically. Thus each ring on the detector represents a small *range* of logarithmically increasing scattering angles. The ring detector is shown in the inset, which also shows the hole at the center of the rings. The main laser beam passes through this hole and is detected by a photo-diode placed behind the ring detector. This provides the optical transmissometer function. It can be seen that the scattered light sensed by the rings undergoes attenuation. It is to correct for this attenuation, that the transmissometer photodiode behind the hole in the ring detector has been employed. Fig. 1b shows the scattering signature, per unit area of particles of two distinct sizes, across these detector rings. The scattered optical power due to large particles peaks at small angles (inner rings), and vice versa. Since the magnitude of scattering is linear with particle numbers, the total optical power<sup>2</sup> distribution sensed by the detector rings is simply the sum of the contributions from each size class, weighted by the concentration in that size class.

<sup>2</sup> The use of the term energy is frequently encountered in particle sizing literature with the laser diffraction method. Strictly speaking, the photosensors respond to optical power in  $\text{W}/\text{m}^2$ . The use of the term energy is probably explained by the implied integration of optical power in angles. We choose the rigorous term power throughout this paper.

Thus, the optical power distribution on the ring detector constitutes the essential information on particle size distribution. The conversion of this power distribution to size distribution involves a mathematical inverse. The procedure employed by us is described in Appendix A. We note in passing that the small-angle scattering thus measured by the instrument is a representation of the optical *volume scattering function* (VSF). This quantity is of interest in underwater light propagation.

The range of sizes of particles that can be observed by this system is established as follows. The largest observable particles are those that put the peak of their scattering at the innermost detector ring. Similarly, the smallest observable particles are those that put their power maximum at the largest rings. Since the rings are logarithmic in radii, thus arranged for mathematical reasons, and since it is obvious that the size classes be chosen so that each size class corresponds to a matching ring, it follows that the size classes are also separated in a logarithmic order. Furthermore, as each ring itself observes scattering over a small sub-range of angles, it follows that each ring also observes a sub-range of particle sizes. The inner radius of a ring corresponds to the largest particles, whereas the outer radius of the ring corresponds to the smallest particles in the corresponding size sub-range, or *size class*. The relationship between the center of each size class  $a_c$  and the corresponding center of the matching detector ring  $\theta_c$  is related to the optical wave vector  $k$ , as:

$$ka_c\theta_c = \beta_{\text{opt}} \quad (4)$$

We have selected the constant  $\beta_{\text{opt}}$  to be 2; (for details, cf. Agrawal and Pottsmith, 1993). For example, if the minimum angle at which scattering is observed is 0.85 mrad, the largest diameter of particles that can be observed with a 0.67 nm wavelength laser is 500  $\mu\text{m}$ .

The inversion of power distribution sensed by the rings produces area distribution of particles (see Appendix A). From the area distribution, the volume distribution of particles is obtained by simply multiplying the area in any size class by the median diameter in that size class. The total volume concentration in the sample can be obtained by summing this volume distribution. In this manner, the true total particle concentration of particles  $\sum C_n$  is obtained, regardless of particle density or size distribution. It

also follows that since the size distribution is measured, the calibration of the measurement of total suspended volume of particles is not affected by a change in size distribution of the particles. The instruments can be tested to this standard in the laboratory, where sphericity and homogeneity of particle composition is easily assured. A crucial test of this idea is to examine experimentally, if the relationship between known volume concentration in a laboratory preparation, and the reported concentration falls on a *common single straight line for different particles and suspensions*. We present such data later in this paper. Now, the ratio of the total particle volume to the total particle area is defined as Sauter Mean Diameter, SMD. Thus, the data permit an estimation of SMD also. Last, from the mismatch in the scattered power distribution data and the fit of the inverse, one has an estimate of the error in the size distribution.

We have deliberately insisted on the use of the term ‘volume concentration’ in this work, rather than mass concentration, as the quantity delivered by laser diffraction instruments. This is to emphasize that neither this nor any of the other methods mentioned earlier obtains any information about particle mass density. However, the uncertainty in mass density of particles is only of about a factor of 3 (density for silica being 2.8, and for biogenous particles, nearly 1). In contrast, the errors due to imprecise knowledge of size can reach far greater magnitudes as sizes in nature vary far more widely than by a factor of 3.

Finally, whereas the calibration of laser diffraction methods is largely insensitive to particle composition, small errors can be expected to arise depending on particle refractive index. The errors become significant when the refractive index of natural particles is vastly different from that used in the computation of the scattering matrix. The use of the correct forward matrix, computed for the correct refractive index of particles can remove this difficulty. However, in nature, the refractive index of scatterers is usually not known. Thus there remains a need to examine the present instruments in the field.

### 3. LISST-100

In Fig. 1, we show the optical schematic common to

the two instruments described in this paper. A 10 mW diode laser is used as the light source. This 670 nm laser is coupled to a single-mode (SM) optical fiber (not shown). SM fiber is used because it preserves the wave-front purity of the exiting light and also because SM fibers enable the tightest possible beam collimation. The SM fibers are angle-polished at the entrance and exit, in order to suppress back-reflection that cause instability of the laser. At the SM fiber exit, a pure, single transverse mode beam emerges. This is coupled to an achromatic collimating lens. Achromats are used because they are also corrected for spherical aberration. Following collimation, a beam-splitter directs a small portion of the laser power to a *reference* beam detector. This reference detector is chosen to be of identical optical responsivity (amperes/watt, A/W) to the one placed behind the ring detector. Its purpose is to detect any drifts in laser power entering water that may arise due to long-term variations of laser characteristics or laser-fiber coupling efficiency. Such changes may also occur due to temperature changes or mode-hopping of the laser. The reference beam power is sensed and stored with each record of the scattering data. The measurement is used to normalize out effects of laser power drifts.

Following collimation, the laser optical path folds and exits a small window into water. The beam diameter in water is 6 mm and the optical path in water is 5 cm. Longer or shorter path may be dictated by the range of optical conditions to be encountered in any experiment. The laser beam illuminates particles in water and then reenters the pressure housing through a larger window. These two windows, being in the optical train, are polished to a very high degree and the air-sides are anti-reflection coated. The direct beam now focuses to a waist at the focal plane where the ring-detector is placed. This detector has 32 logarithmically placed rings. The inner radius of the smallest ring is 102  $\mu\text{m}$  and the outer radius of the largest ring is 10 mm (20 mm in newer instruments). At the center of the ring detector exists a laser-drilled hole to pass the direct beam through the silicon. The transmitted beam power is sensed with a silicon photo-diode placed behind the ring detector. This photo-diode constitutes the optical transmissometer function. The overall sensitivity of the ring detectors is 2.44 nA per digital count. With a typical silicon responsivity of 0.4 A/W, this implies an optical

power resolution of nearly 6 nW. The amplifiers have a 3 dB low-pass cut off at 10 Hz. The low bandwidth is employed to reduce shot-noise of optical detection (Yariv, 1988). Overall electronic noise is less than one count. The fastest rate at which scattering distributions can be acquired is 5 Hz, limited only by the low-power data-acquisition computer.

The amplified outputs of the ring detectors in all instruments are stored in memory on board the computer controlling each instrument. A typical data record consists of the following: 32 ring outputs, laser power transmitted through the water, battery voltage, one external channel, reference laser power, pressure, temperature, and two auxiliary parameters (generally time counters, e.g. hour and minutes). Each data word is a 2 byte, 12 bit sample. The on-board computer is programmable to take scattering distribution samples at any arbitrary schedule, but not at a higher than 5 Hz rate. For all cases, a background scattering distribution is measured and stored. The source of this scattering is micro-roughness on optics. This background is termed *zscat*. It is shown in Appendix A that the measured data from particles is attenuated by the factor  $\tau = \exp(-cl)$  in accordance with Beer's law, where  $c$  is the beam attenuation per meter and  $l$  is the optical pathlength,  $l = 5$  cm. The attenuation is estimated from the ratio  $\tau = T/T_0$ , where  $T$  is transmitted power, normalized by its value  $T_0$  when the background measurement is made using highly filtered pure water. The corrected scattering from a sample of water is then obtained as (see Appendix A for details):

$$s = [\bar{d}/\tau] - \text{zscat} \quad (5)$$

where  $\bar{d}$  is the 32-element scattering distribution vector as recorded from a sample containing particles under measurement, and the quantities  $s$ ,  $\bar{d}$  and *zscat* are in digital counts. The vector  $s$  is then corrected for the non-ideal detector responsivity correction factor  $\bar{\mathbf{D}}$  (explained below) to produce a fully corrected scattering distribution  $S$ , still in digital counts:

$$S(i) = s(i)\bar{\mathbf{D}}(i) \quad (6)$$

From this final corrected scattering, the volume distribution is constructed as an inverse,  $\text{INV}(S)$ , (see Appendix) which upon division by the *volume*

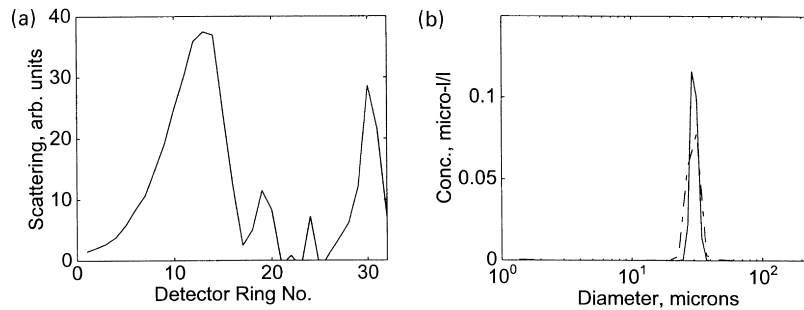


Fig. 2. (a) Scattering signature of single-size (30  $\mu\text{m}$ ) particles; data collected with the 32-ring LISST detector. (b) Volume distribution constructed with 2 methods: --- is the model-independent method, solid line is log-normal best fit distribution.

conversion constant  $C_v$  (see below) yields the finally desired quantity, volume concentration:

$$C_n = \text{INV}(S)/C_v \quad (7)$$

This is the desired quantity of Eq. (1).

### 3.1. Detector calibration

Two categories of calibrations are performed. The first is to measure the overall sensitivity of the electronics and to determine the overall responsivity of the detector. The detector ring inner and outer radii  $r$  follow the geometric dimensions as follows:  $r_i = r_1 \rho^{i-1}$  and  $r_0 = \rho r_i$  where  $\rho = D^{1/32}$  and  $D$  is the dynamic range of the detectors, i.e.  $D = \theta_{\max}/\theta_{\min}$ .  $D$  is 100 for the LISST-100 (200 in newer detectors). This defines detector areas. A uniform light field is produced with an incandescent lamp and a diffuser. The ring detector is placed in this field and the output of each of the 32 rings is recorded after amplification. Ideally, the areas of each ring should be  $\rho^2$  times the previous inner ring. In a uniform light field, the photocurrents should follow this trend. Departures from this trend are saved as the combined detector-electronics gain compensation vector  $\bar{\mathbf{D}}$  used in Eq. (6).

### 3.2. Overall volume concentration calibration

A mixture of known volume concentration of particles,  $V_0$ , is prepared. The background scattering distribution from filtered water,  $z_{\text{scat}}$ , and the scattering distribution from the suspension are recorded. The quantity  $S$  is computed as in Eq. (6) above. Finally,

the volume conversion factor  $C_v$  is determined from:

$$C_v = [\text{INV}(S)]/V_0 \quad (8)$$

It is essential that to be consistent with the presentation above,  $C_v$  be constant, regardless of the particles being examined so long as they are within the range of measurable sizes. The verification of the constancy of  $C_v$ , regardless of particle size distribution is described below.

### 3.3. Laboratory tests

The objects of the laboratory tests are three-fold. They are to determine: (i) if, given scattering data from a known-size particle suspension, the instruments retrieve it correctly; (ii) if, given a distribution of sizes present in a standard suspension, the instruments retrieve this size distribution from the data; and (iii) whether, regardless of the size distribution of particles used, the instrument retrieves the correct total concentration,  $\sum C_n$ , of particles in a suspension.

The first tests were carried out using single-size 30  $\mu\text{m}$  polystyrene spheres, obtained from Duke Scientific, Inc. (Palo Alto, California). The index of refraction of the polystyrene is 1.596; that for glass is 1.5. The forward matrix is computed for an index of 1.5 corresponding to glass, and is intended for general-purpose use for natural siliceous particles. Scattering signature of the 30- $\mu\text{m}$  spheres is shown in Fig. 2a and the size distribution is shown in Fig. 2b. The two inversions shown in Fig. 2b are based on two different methods: a model-independent method and a best fit SM lognormal or Gaussian form. Note that the two methods are generally

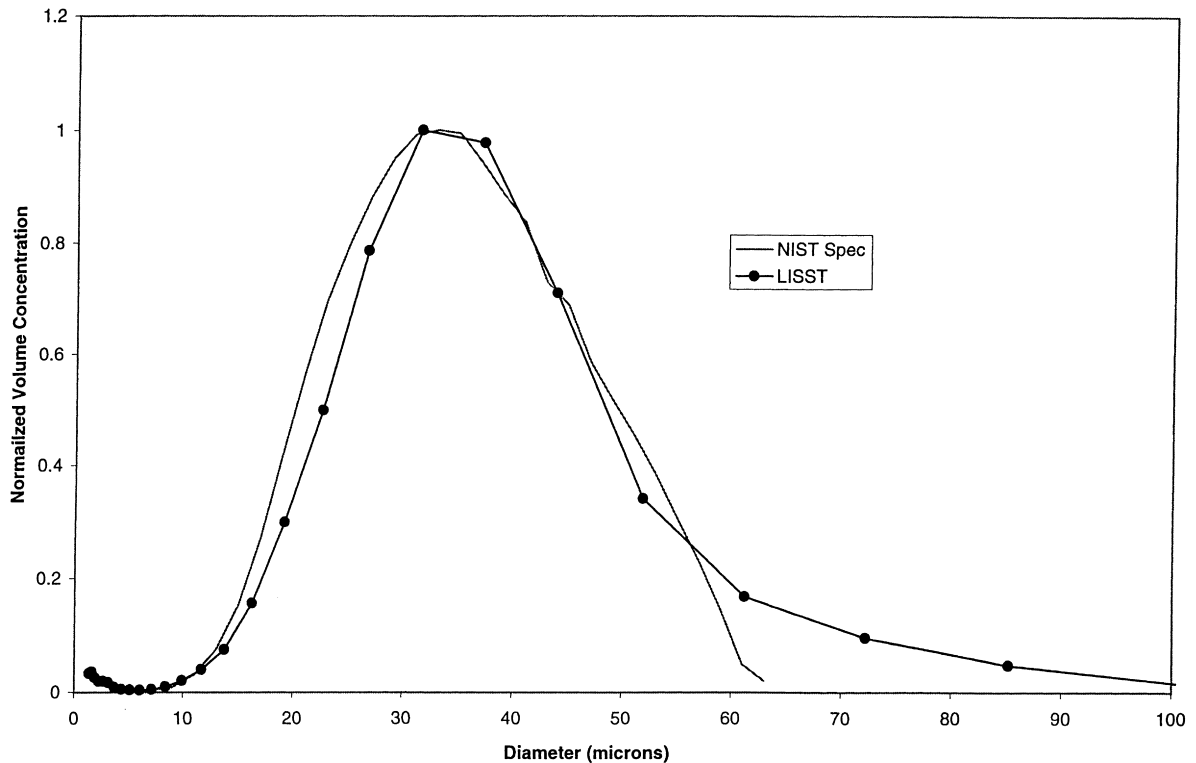


Fig. 3. Results of a test with a standard glass sphere powder, NIST-1004, available from the US National Institute of Standards and Technology.

consistent, although the assumed lognormal form inverse is narrower and therefore offers better resolution. When there is a priori knowledge of a distribution being narrow, an assumed form method can be applied.

In Fig. 3, we compare our estimates of the size distribution from the known size distribution of glass spheres available as standards from the US National Institute of Standards and Technology (NIST). Fig. 3 shows the NIST-specified size distribution against our estimate. The agreement is found to be satisfactory. There is no definite explanation for the extended tail in our estimate. It is most likely due to the limitation of resolution of the method (see the next paragraph). Figs. 2 and 3 serve as essential calibration tests. Note that the small difference in height and width between specified and recovered size distribution simply conserves the total volume for the two solutions.

The resolution of these instruments is the subject of

much complex mathematical research. The noise of measurement and conditioning of the kernel matrix (see Appendix) ultimately affect the resolution. Typically, no more than about 8–10 distinct sizes can be resolved in this method when the size range spans 100:1. We illustrate the resolution with laboratory data obtained using polystyrene spheres of known sizes, Fig. 4. Particles of narrow distribution but in different sizes were added into a single chamber and the scattering was recorded and inverted. It can be seen that despite the very narrow size distribution of the particles employed (1% spread in sizes) the inversion is not a single size-bin result. However, the 5 size classes could be clearly resolved. Notably, recent work by Traykovski et al. (1999), using the LISST-100, reported a lower resolution. This was due to the use of a regularization method inversion algorithm provided to them earlier. This earlier algorithm used a least squares best fit with the added constraint of smoothness. The newer iterative algorithm based on

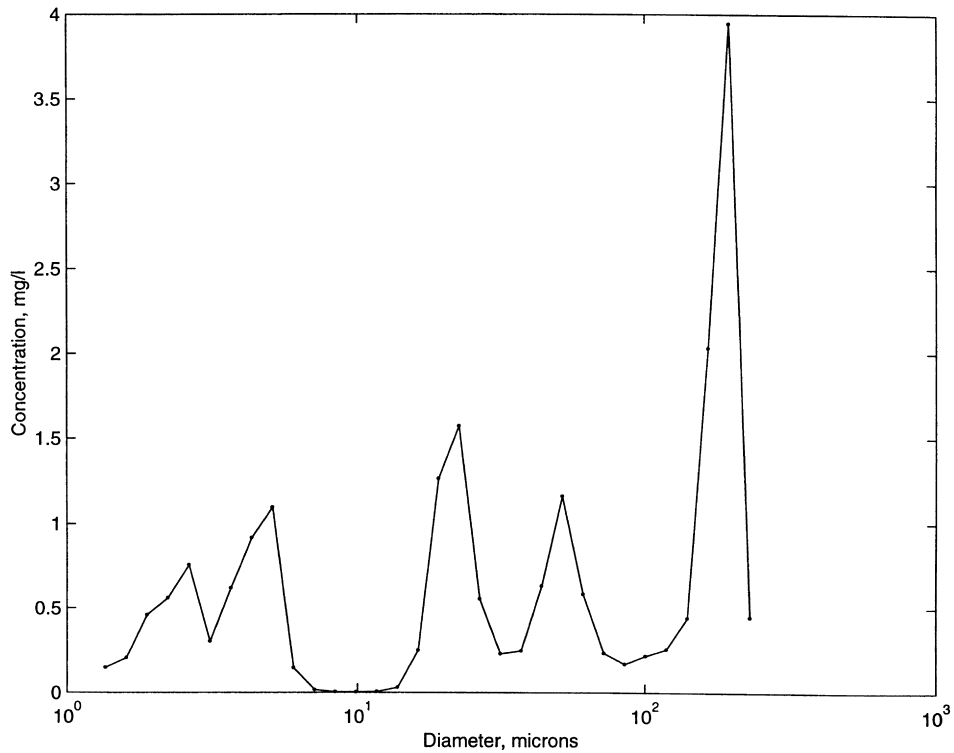


Fig. 4. The size distribution recovered when a number of single-size particles were used as scatterers. In this case, narrow distributions (1% width) of particles of 2.5, 5, 20, 50 and 200  $\mu\text{m}$  were added. All sizes are clearly resolved.

Chahine's method, (Riley and Agrawal, 1991) is employed to get the results of Fig. 4; it clearly delivers a higher resolution.

For the third test, that is, does the method retrieve the true real total concentration of different suspensions of particles, regardless of their size distribution, we show data in Fig. 5. In this case, we have several different powders of polystyrene particles from Duke Scientific, Inc. (Palo Alto, California). Two other samples of natural sediments, provided as calibration standards used by the US Geological Survey were also included in this plot, labeled AC fine and AC coarse. These are naturally occurring powders employed in the manufacture of ceramics for spark plugs. These powders were dry-weighed and dispersed with an ultrasonic device before scattering distributions were recorded and analyzed. The results are displayed as weighed vs. reconstructed total volumetric concentration of particles, with appropriate account having been taken of the known material mass density. The

reconstructed total concentrations are estimated using the LISST's size-based information. The results show a consistency between weighed actual concentrations and optically retrieved estimates to within  $\sim 20\%$  for all powders, despite their typical size varying by an order of magnitude. This constitutes the essential proof of constant calibration of this instrument for measuring total sediment concentration, independent of the size of underlying suspensions.

We now remark on the consequences of data contaminated by particles outside the range of measurements, i.e. for particles of sizes too large or too small. Referring back to Fig. 1b, particles *smaller* than the measurement range would produce a scattered light distribution peaking at angles larger than  $\theta_{\text{max}}$ . In this case, their contribution to the detector rings will be peaking at the outermost ring, so that they will be interpreted as particles in the finest size class. In contrast, particles *larger* than the largest measurable will put most of the scattering at angles

## Results from Chahine, March, 1998

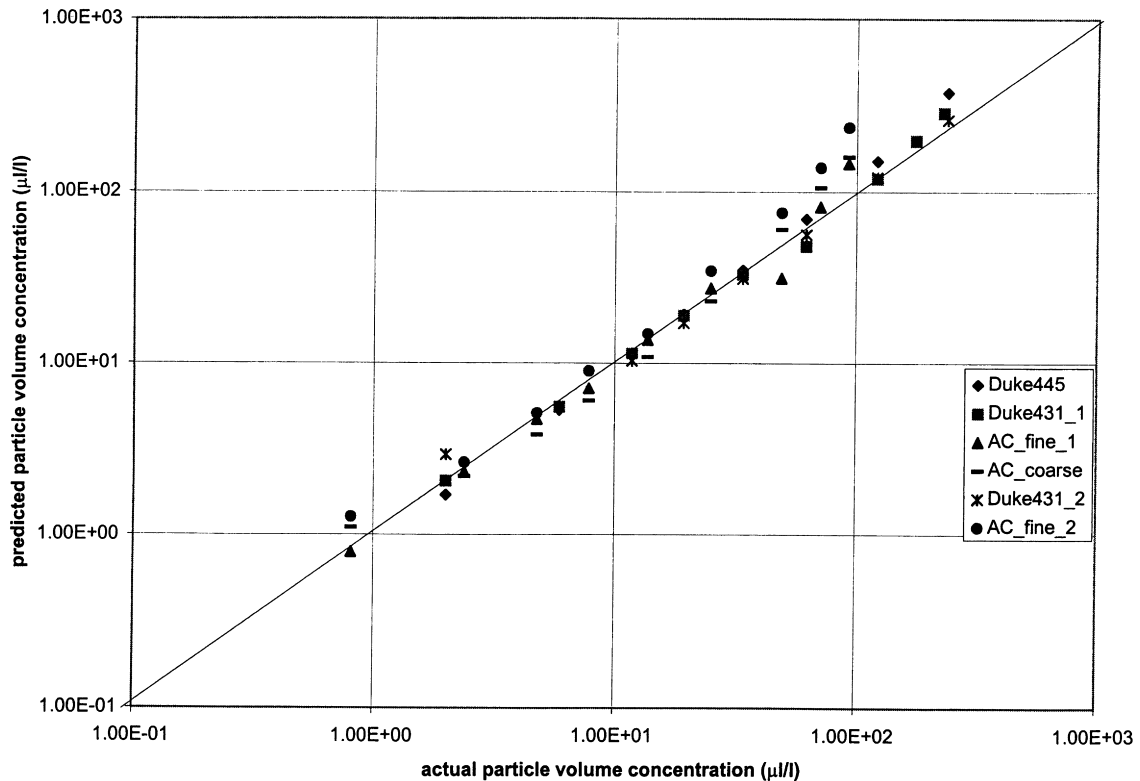


Fig. 5. The relationship between known and measured total concentration of suspended particles for several different powders. A single linear fit indicates the independence of calibration from size-distribution. At high concentrations, departure from the 1:1 line arises when beam transmission drops below about 30%, i.e. as multiple-scattering effects become increasingly significant.

smaller than  $\theta_{\min}$ . A 'leakage' will now result primarily at the smallest, inner rings, thus these particles will be interpreted as additional large particles. It might thus be expected that whenever particles outside the measurable range are present, their scattered power would *leak* into the nearest size particles that are within the range of measurement. However, in these cases, the method fails to maintain correct calibration for total suspended concentration.

#### 3.4. Small scale turbulence and small number statistics at large particle sizes

The theory of turbulence predicts that passively advected scalars (e.g. particle concentration) exhibit small scale structure similar to fluid motions. In other

words, variability of  $C_n$  can be expected at scales down to micro-scales. The laser beam in Fig. 1a crosses several such structures, effectively integrating the concentration along a line of finite thickness. Thus, the observed particle concentration will exhibit noise-like random variations caused by the small-scale structure within the laser beam. Furthermore, just as velocity averaging times must take into account the integral time scales for velocity (given by  $z/U$ ), so also to obtain true mean concentration of particles, averaging of concentration over several integral time scales is necessary.

An unfortunate consequence of the relatively small sample-volume dimensions of the laser diffraction instruments (typical volume is  $2 \text{ cm}^3$ ) is that when the number density of particles is small, as is typical

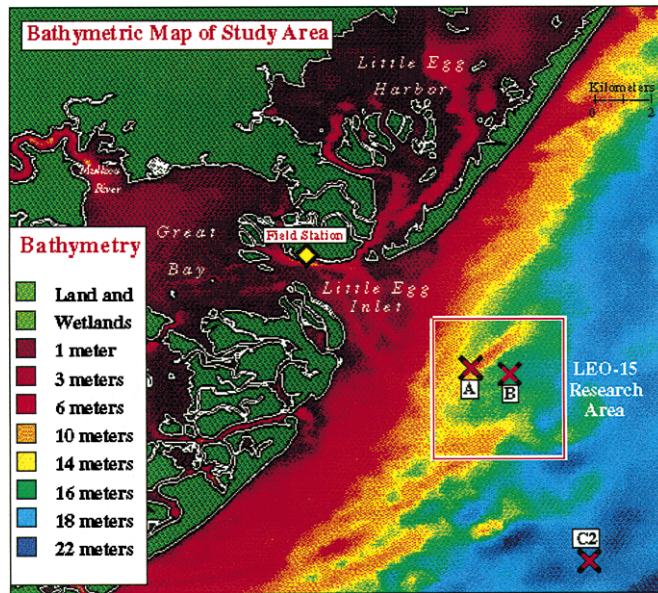


Fig. 6. The LEO-15 site off Atlantic City, NJ. The measurement location was in 15 m depth, at site noted as B, roughly 6 km offshore.

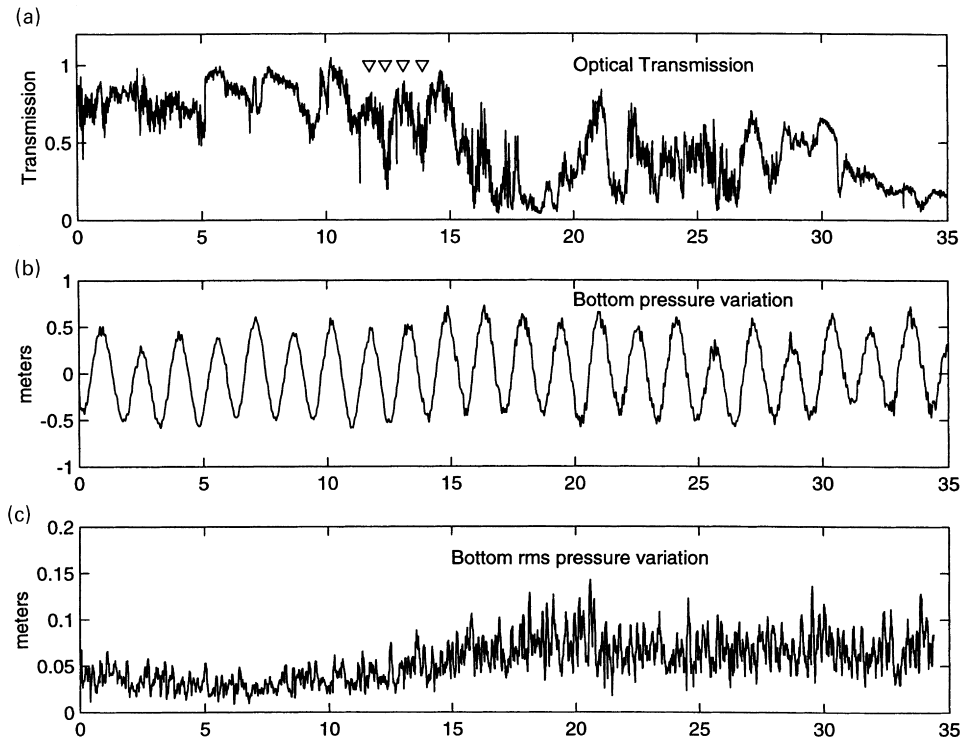


Fig. 7. (a) The optical transmission; (b) tide; and (c) rms wave-induced bottom pressure. The abscissa is days after launch on 8 August 1995.

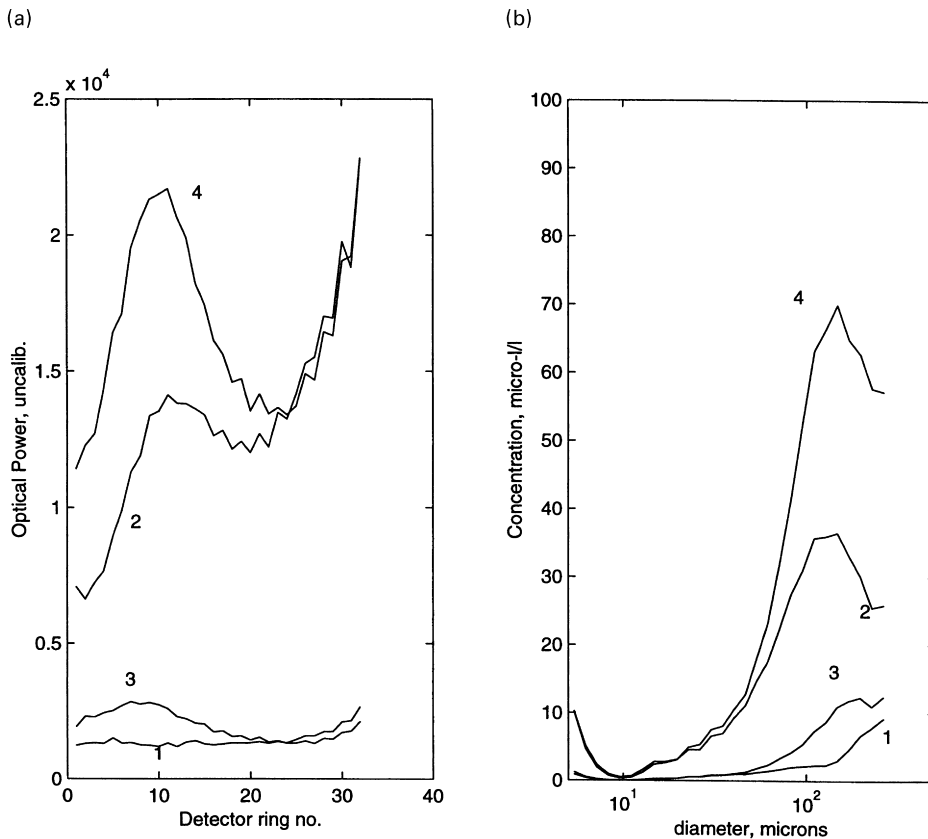


Fig. 8. (a) Scattering at selected times during an event (indicated by inverted triangles in Fig. 7a); (b) volume distribution corresponding to the data of (a).

for the largest particles (e.g. flocs or marine aggregates), statistical variability of the particle number in the sample volume itself becomes large. In interpreting field data, it is important to bear this in mind. Of course, averaging over several scans, in effect, increases the sample volume size and thereby reduces this variability.

### 3.5. Field tests

We illustrate data from a field experiment carried out on the New Jersey coast at the LEO-15 Observatory maintained by the National Undersea Research Program. The program is funded by the US National Oceanic and Atmospheric Administration (NOAA). Fig. 6 shows the location of the experiment, which is roughly 4 miles offshore, east–northeast of Atlantic City, New Jersey. The water depth is 15 m and the

topography is a dynamic field of sand ripples. In this bottom boundary layer experiment, a suite of instruments was placed to record currents, bottom topography, and suspended sediment concentration and size distributions. The data that we have selected will illustrate the point that the size distribution responds to local forcing through resuspension, so that as the forcing weakens, so does the concentration of the larger size classes.

Two LISST-100 instruments were placed on a single tripod in this experiment at the LEO-15 site. The two instruments were placed at heights-above-bed of 0.3 and 1.5 m. The optical transmission and pressure measured by the auxiliary sensors on the LISST (showing tides) during the experiment are shown in the top two panels of Fig. 7. On the bottom panel, we show the pressure variance as an indication of surface wave activity. The pressure signal on the

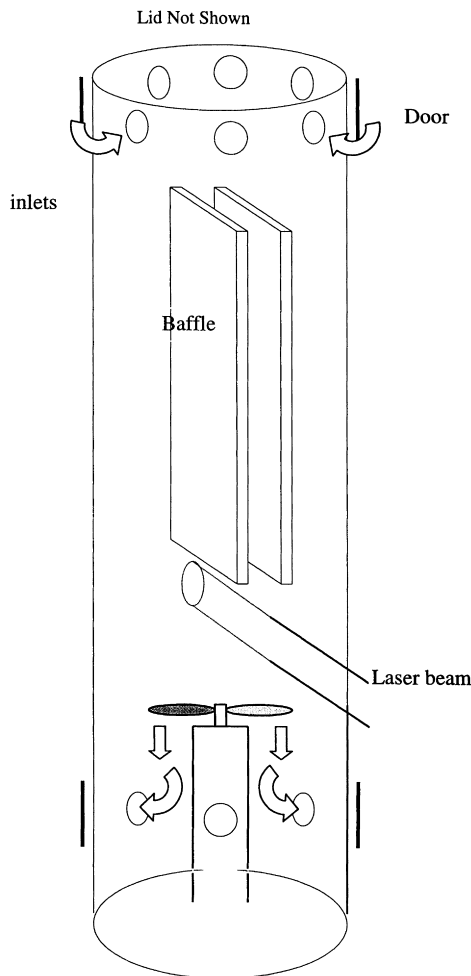


Fig. 9. The settling column, along with the propeller and sliding doors. Top and bottom lids are not shown. The column is 5 cm in diameter, and 30 cm tall from the inlet to the laser beam.

bottom related to gravity waves is computed as follows. As pressure was sampled at 15 min intervals, tides and surface waves are separated by first high-pass filtering the pressure record. This provides samples of wave-height at the 15 min intervals. These realizations of wave-height are then squared and convolved with an 8-point top-hat filter to generate smooth estimates of mean-square wave-height during the course of the experiment. The arrows on this optical transmission record indicate the duration from which scattering distribution records are analyzed. It is seen that when the optical transmission

is higher (clearer water, curves 1&3 in 8a), the maxima of the scattering curves occur at the innermost rings even though there is relatively less scattered light. This corresponds to large particles in the size distribution (curves 1&3, 8b). At the valleys in the transmission curve (Fig. 7, top panel, second and fourth inverted triangles), a lot more scattered light is seen but with a peak at somewhat larger angles. This implies smaller particles (curves 2&4, Fig. 8a and b). The data suggest that during weaker forcing, when large, dense primary particles can not be supported by turbulence, flocs must form with the characteristic strong scattering at the smaller angles. These might break up with stronger forcing, when also, an additional supply of sediment is made available to the water column. We have observed similar patterns in the Coastal Mixing and Optics experiment (Agrawal and Traykovski, 2000).

Theory has predicted, as described in the introductory sections of this paper, that vertical gradients in concentration can be expected for particles whose settling velocities approach  $ku_*$ . Such observations are possible with two vertically placed instruments. The use of vertical gradients in size distribution using the (Rouse, 1937; #1255) formulation suggests possibilities of inferring the particle settling velocities. We shall examine the data from this standpoint in a future publication.

#### 4. LISST-ST

This instrument for measurement of the size-dependent settling velocity distribution without assumption of particle density is similar to the LISST-100. The optics end of the instrument is enclosed in a settling tube of 30 cm length. The settling column, Fig. 9, which is enclosed in this 5 cm diameter settling tube, consists of a 5 cm × 1 cm wide × 30 cm tall rectangular volume. The rectangular column reduces flow Reynolds number significantly from the round tube for the draw-in velocities. This feature is incorporated to assure faster suppression of turbulence in order to obtain good estimates of the rapidly falling larger particles. The settling tube has openings at the top and bottom. Two motors are incorporated in the system. One motor operates the doors and the second powers a propeller in the settling tube, placed just

below the laser beam. Vertically sliding doors with radial 'O'-ring seals are used to open and close the doors. The cycle of operation is as follows: before closing the doors, the motorized propeller in the settling tube is powered up. Its function is to draw in a new sample. The sample enters the settling tube at the top, and is blown out at the bottom. A short-time (4 s.) is allowed to elapse after the propeller power is turned off. This ensures filling the tube with new fluid, unaffected by propeller motion. At this time, the doors are rapidly closed, in about 50 m s. This begins the settling experiment. Data are taken at logarithmically scheduled sampling intervals. In all, 83 scans are saved over a day. At the end of the settling experiment, the propeller is powered so that its vigorous turbulence cleans the settling column and the optics windows. The doors are opened, so that the propeller blows the stirred water out, and at the same time draws in a new sample. This begins the next cycle of data acquisition.

Consider now the evolution of size distribution at the optics block in the lower part of the settling column where the laser senses size distribution. In the case of a homogeneous suspension, i.e. all particles having the same mass density, each particle size class will traverse the 30 cm settling tube at its own unique settling velocity, determined solely by diameter. Assuming that the settling column was filled with a well-mixed sample of water, the concentration history of any single size class of particles can be expected as follows. As particles of this size class settle, at some point in time, those particles that were at the top of the settling column reach the laser beam. Until this time, the concentration observed at the laser beam can be expected to be constant, equal to the fill-up concentration. Any apparent variations in concentration prior to this time can arise due to imperfect mixing and small number statistics of the particles. Further settling causes the particles to fall through the 6-mm diameter laser beam leaving no more particles of this size to produce laser scattering. Thus, over a duration corresponding to the time to fall through the laser beam, the concentration for any size class of particles will go from its natural value at fill-up, to zero. Thus, both the onset of the decline in the idealized constant concentration history, and the length of duration of the sloping region will be uniquely related to a particular particle size. This is

the idealized expectation. In reality, a few effects complicate observations. First, natural particles are seldom of a homogeneous composition, so that a variation in particle density will cause a smearing of the concentration profile. Second, the existence of residual turbulence from the fill-in period smears the measurement of settling velocity for the largest particles. A third factor is particularly frustrating, but only in the laboratory: convection currents caused by temperature changes with the cycling of ventilation systems. It is worth noting that turbulence or convective motions must be weaker than the smallest settling velocity of interest, in order to make a correct measurement. Such conditions are difficult to achieve in the laboratory for the smallest particles, whose settling velocities may be a small fraction of a mm/s, in effect setting the limit of measurable small-particle settling-velocity. The requirement that turbulence or convection be much weaker than the smallest settling velocity of interest is fundamental, not specific to any technique. The thin settling column of the LISST-ST is a couple of orders of magnitude thinner than typical other settling tubes, e.g. the ROST device (roughly 30 cm × 20 cm cross-section) employed by Hill et al. (1994), or the INSSEV of Fennessy et al. (1994). The data we show below indicate that, significantly, turbulence in our settling column is indeed fully suppressed so that not only does the water clarity increase monotonically, but also the smallest measurable particles do settle out over a time that is reasonably predicted by Stokes law.

In order for the settling histories to be employed for estimation of settling velocity, it is necessary that the concentration measurements for each size class be totally independent of any other. Smoothing, as often employed in least squares inverse algorithms, works against statistical independence. Thus, one must first ask the question: how many truly independent size classes are derivable from the multi-angle scattering data. In a landmark paper, Hirleman (1987) showed that the answer depends on the conditioning of the forward matrix. Typically, with a 100:1 range of scattering angles, only about eight truly independent size classes can be obtained. Each of these size classes contains particles spanning a size range 1.78:1. We offer this summary view for quick reference; the interested reader may understand the

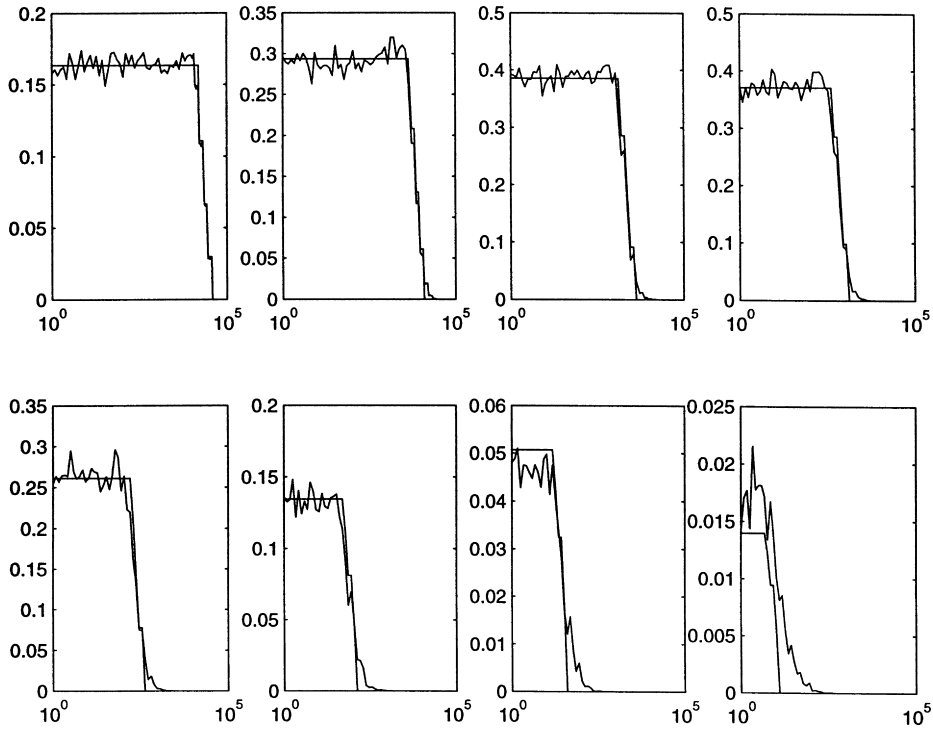


Fig. 10. Results of inverting synthetic data to produce concentration histories of 8 size classes.

relationship between measurement noise and the information content of the data by referring to Hirleman (1987).

To verify that truly independent settling histories are obtained, we present first a synthetic numerical settling experiment. The procedure is employed as follows. An initial, log-normal distribution of particles was synthetically generated, with a mean ( $\mu$ ) placed at size class 12 out of 32 log-spaced size classes between 5–500  $\mu\text{m}$ , and a width ( $\sigma$ ) of 8 size classes. By not including noise in the initial size-distribution, we are implying a well-mixed suspension. With this starting condition, time histories for each of the size classes were synthesized using the Stokes settling formula. In this manner, the time history of the size-distribution itself was synthesized. This was used along with the Mie calculated matrix to synthesize the history of scattered optical power distribution across the rings, as  $\bar{E}^i = \bar{K} * \bar{N}^i$  where the superscript  $i$  refers to the sample size distribution at time step  $i$ . Now, the synthetic scattered power distribution  $\bar{E}$  was contaminated with zero-mean

multiplicative white noise, which represents the consequence of averaging a finite number of scans across the rings. Thus  $\bar{E} = (1 + \epsilon) \bar{E}$ .  $\epsilon$  was generated from a zero-mean, uniform random number generator. The magnitude of the zero-mean, white noise  $\epsilon$  was adjusted for several cases. In Fig. 10 we show the history of the recovered size distributions. Note that the settling out times of the size classes are obviously represented by synthetics, despite the noisy size distribution reconstruction. The implication is that at least, numerically, there is no difficulty in reconstructing the history for 8 size classes. The purpose of inclusion of this result is simply to ensure that the 8-size class approach is not fundamentally limited by mathematical problems.

As a laboratory test of this device, we have employed NIST traceable glass sphere powder. This powder contains particles in the size range 1–85  $\mu\text{m}$ , as specified by NIST. A laboratory test was carried out in which a well-mixed suspension of these spheres was introduced into the settling column of the LISST-ST. Particles were introduced while the

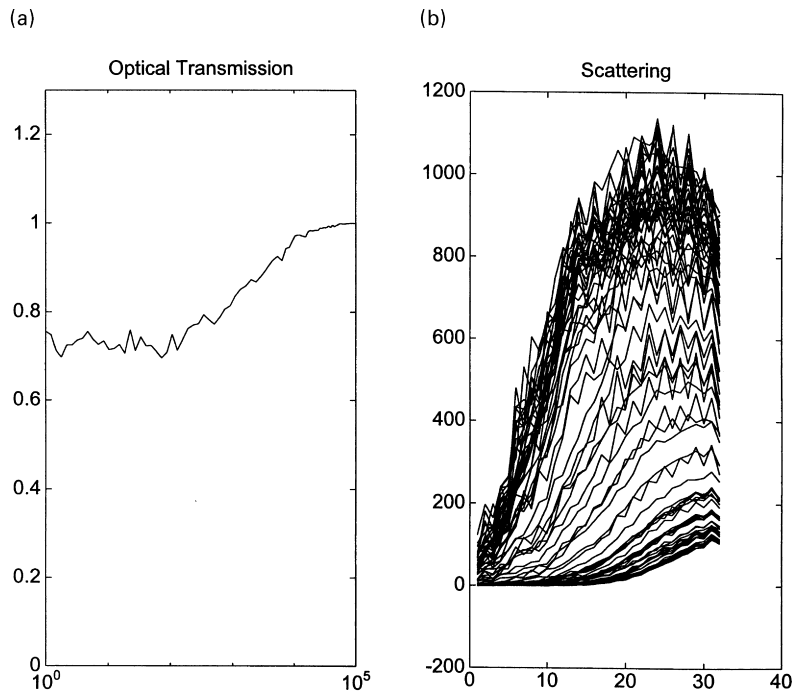


Fig. 11. History of: (a) optical transmission; and (b) scattering distribution during the settling experiment using glass spheres.

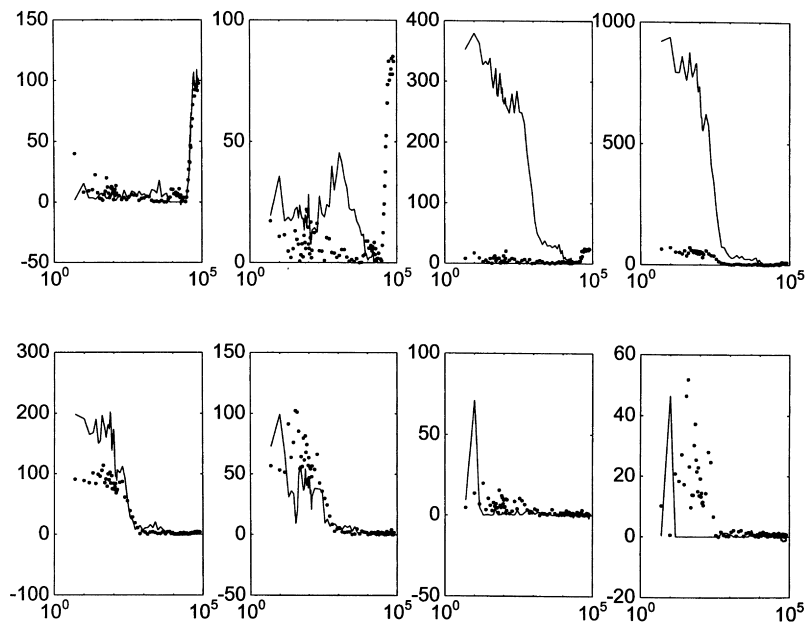


Fig. 12. Concentration history of 8 size classes for the NIST standard glass spheres. The solid lines show the estimates of concentration, the dots indicate error of the estimate. When error exceeds the estimates, the size class history is fully discarded.

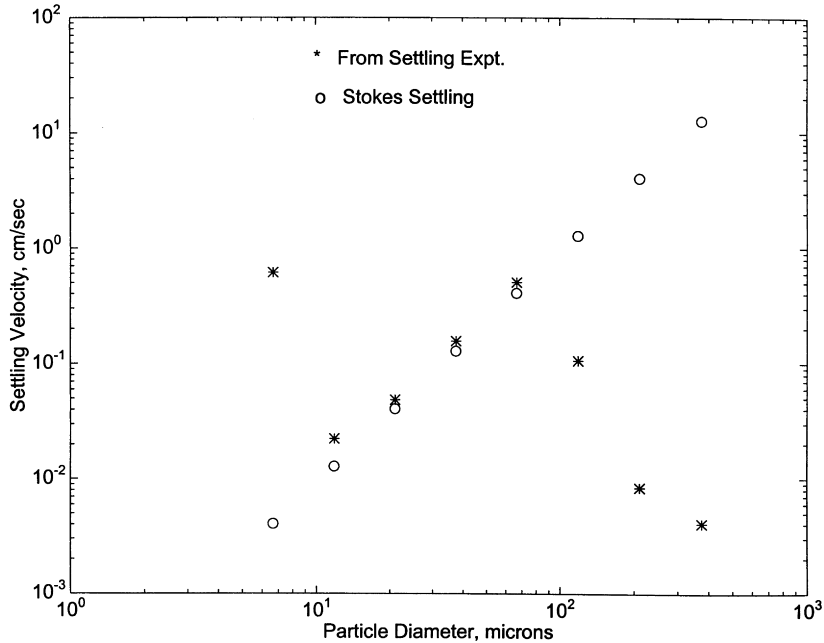


Fig. 13. Estimates of settling velocity of glass spheres, compared with Stokes settling. Note that as the size distribution is quite narrow (Fig. 3, and also Fig. 12), several size classes are unpopulated. This produces noisy estimates for the nearly empty size bins. As a result, the settling velocity can be estimated for only size classes 2–5.

instrument was submerged in an approximately constant temperature tank. Scattered optical power distribution on the detector rings was recorded on a logarithmic time schedule, with samples acquired a few seconds apart initially, and several thousand seconds apart toward the end. The settling experiment lasted a full 24-hour duration. During this time, 83 scans were stored. As usual, the scattering signature of the suspension at any of the 83 scans was calculated by subtracting the  $z_{scat}$  from the recorded data. The optical transmission and scattered optical power history are shown, respectively, in Fig. 11a and b. The water monotonically gets clearer as particles settle. Similarly, the scattering signature during the course of settling shows a shift in the location of the peak to the right, i.e. to the larger rings, as would be expected with reduction in large particles that scatter into small angles. These data are inverted using an 8-size class inverse. Fig. 12 shows the settling history. In this case, note first that the first size class (5–8  $\mu\text{m}$ ) is empty as very little mass was present in the powder. The size classes 3–5 contain the bulk of the particles, and these are displayed in c–e. The dots on each plot

show the error of the estimate, computed from the inverse of the data and the fit. Thus, when the noise level represented by the dots is small compared to the signal level, settling velocity estimates from these data can be trusted. This criterion serves as a guide for interpreting the settling velocity estimates. It follows that again, there is negligible mass in the larger size classes, as is evidenced by large noise spikes in f–h.

The settling history of each size class is converted to a settling velocity following an optimization procedure. Assuming homogeneity within a size class, the problem of estimating the settling velocity becomes a one-parameter optimization problem. Consider the settling time for particles in size class  $n$ . This size class contains particles of sizes  $a_{\min}\rho^{n-1}$  to  $a_{\min}\rho^n$ . Now, a single idealized concentration is constructed that has a constant concentration for the duration  $30\text{ cm}/w_{f,n}$ , followed by a linearly sloping concentration as the particles fall through the laser beam, and a zero concentration thereafter. The sloping section has a duration such that, the smallest to the largest particles in the size class fall through the 6mm beam in this

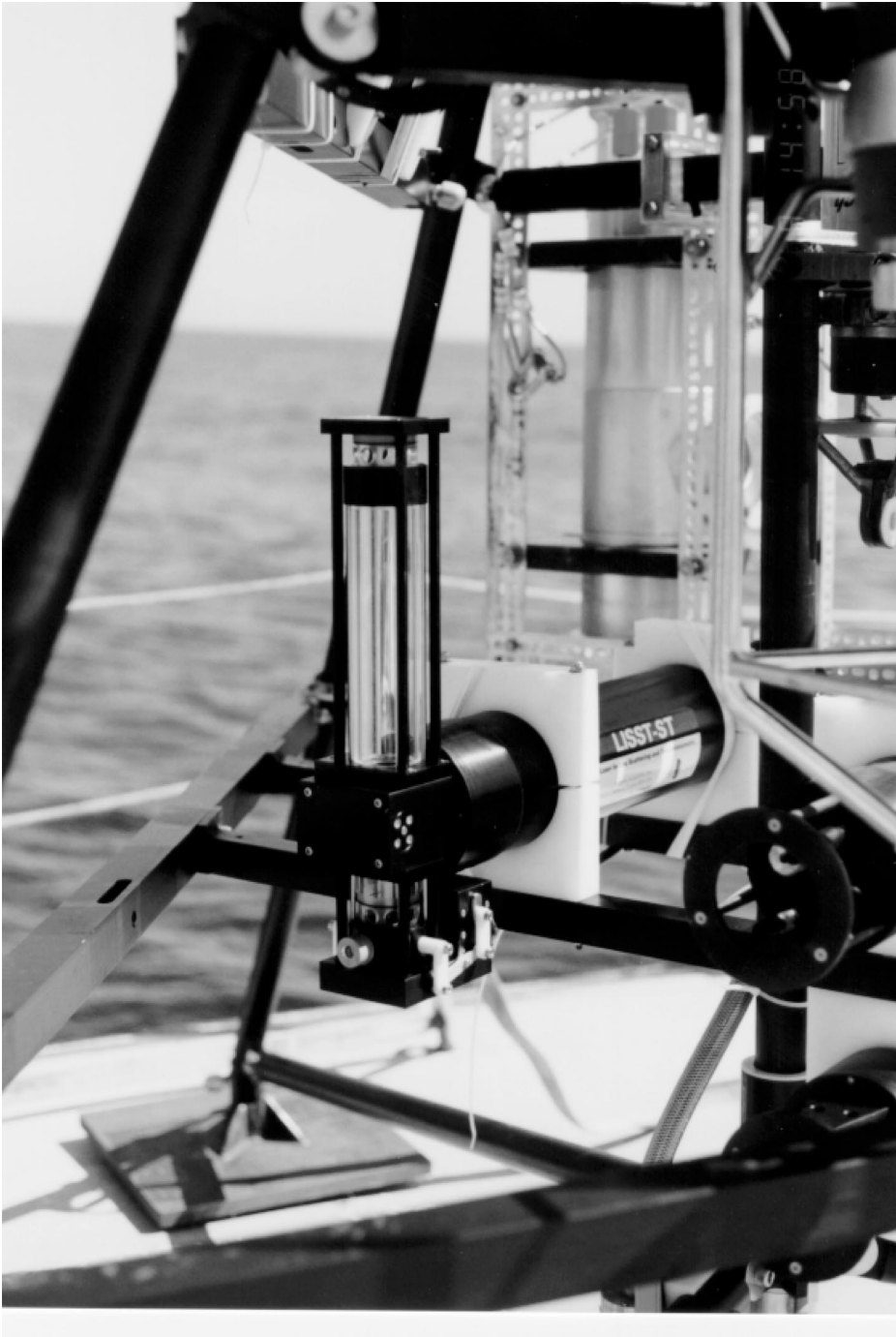


Fig. 14. Photograph of the LISST-ST instrument shown mounted on the tripod used at the LEO-15 site.

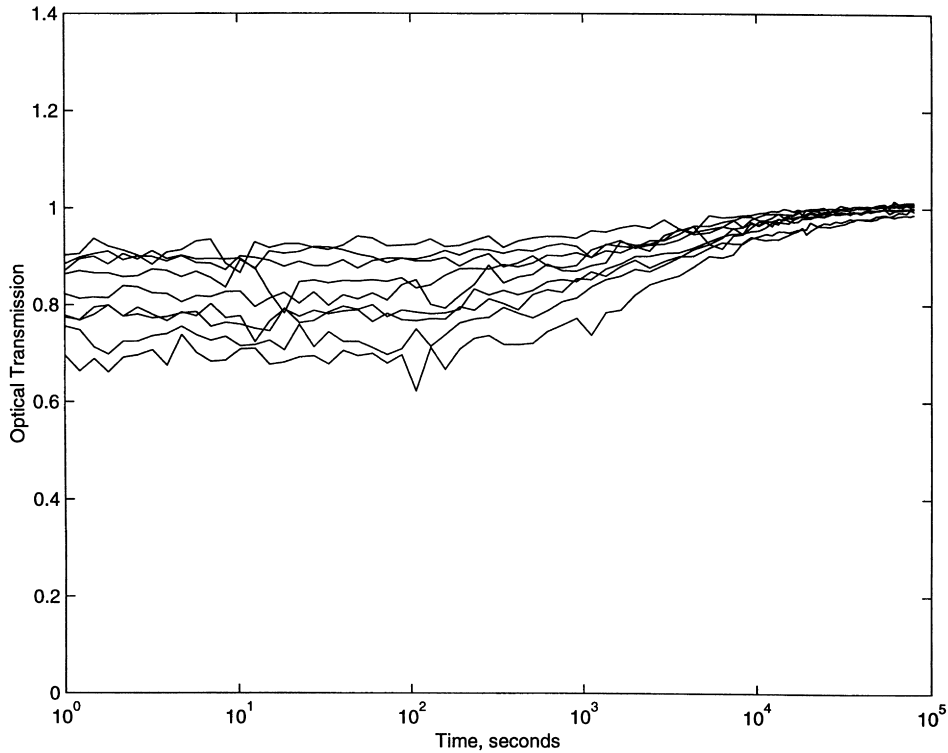


Fig. 15. The optical transmission for 10 successive days.

time. This duration begins at  $30/w_{f,n}$ . The smallest particles in the size class fall through the laser beam over a time equal to  $6 \text{ mm}/w_{f,n-1}$  whereas the largest particles within the size class fall through over a time equal to  $6 \text{ mm}/w_{f,n}$ . Thus the length of the sloping part of concentration history is expected to be  $6/[1/w_{f,n-1} - 1/w_{f,n}]$ . In effect, the square parentheses arise due to the finite size-width of size class  $n$ . Now since  $\rho = 1.78$  and settling velocity can be reasonably expected to follow Stokes' law, the settling velocities will vary within a size class by  $\rho^2 = 3.2$ . Thus, the break in the sloping duration will begin at some time  $T_B$  and end at  $3.2 T_B$ . The difference,  $2.2 T_B$  is the length of the sloping region.

One now finds a  $T_B$  which minimizes the mean-square difference between the idealized and normalized history of any size class. Mathematically, this is expressed as follows. Let the time history of concentration in size class  $n$  be called  $C_n(t)$ , then one defines an idealized history by the function  $\Phi(t)$  such that it is constant for time  $T_B$  equal to  $30 \text{ cm}/w_{f,n-1}$ , gradually

decreases to zero over the time it takes particles of sizes in the size-class to fall through  $6 \text{ mm}$ , i.e.  $2.2 T_B$  and is zero thereafter:

$$\begin{aligned} \Phi(t) &= 1/T_B \int_0^t C_n(t) dt && \text{for } 0 < t < T_B; \\ &= \Phi(T_B) - (t - T_B)/2.2T_B && \text{for } T_B < t < 3.2T_B; \\ &= 0 && \text{for } t \geq T_B \end{aligned} \quad (9)$$

The best estimate of settling time  $T_B$  is found by minimizing the least square difference of the history with the idealized history  $\Phi(t)$ , i.e.:

$$d/dT_B \{ [C_n(t) - \Phi(t)]^2 \} = 0; \quad (10)$$

The procedure is implemented numerically. The solutions  $T_B$  for each size class are used separately to estimate the settling velocity for that size class. These data are shown in Fig. 13. It can be seen that the experimental data match Stokes settling to an error of nearly 20%. We are not certain as to the cause of

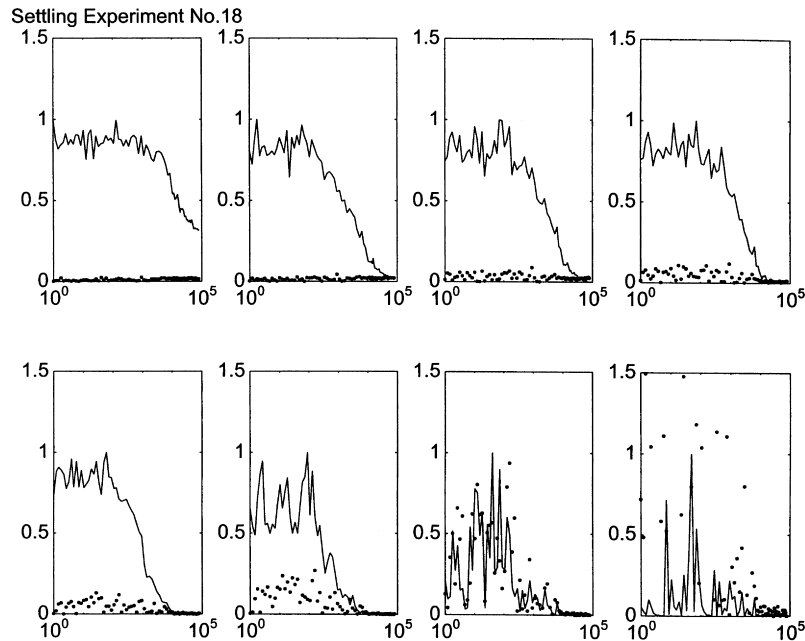


Fig. 16. Concentration history for the 8 size classes during one of the 10 experiments shown in Fig. 15.

the apparently small bias, but we speculate that the bias results from the observed longer than theoretical sloping region of the concentration history, which in turn, probably is caused by convective currents in the laboratory excited by ventilation.

A final comment regarding estimation of settling velocities with a sampling system concerns floc break-up. Gibbs and associates have published a series of articles on floc break-up (Gibbs, 1982; Gibbs and Konwar, 1982, 1983). These articles concern themselves with breakage of flocs in the course of, respectively, analysis with a particular optical blockage instrument, due to pipetting, and during Niskin bottle sampling. We have not been able to quantify such effects in this study. A noteworthy detail is that the sample water is drawn through 12.7 mm holes at the top of the settling column.

#### 4.1. Field tests

The *field* settling velocity data presented in this paper were obtained in the NURP program already mentioned in an earlier section, although the current data were acquired in a deployment at the site in December 1997. The LISST-ST was mounted on a

tripod and deployed at the approximately 15 m depth for bottom boundary layer measurements from a tripod. The instrument is displayed on the tripod in Fig. 14. A settling experiment was begun each midnight and lasted most of the 86,400 remaining seconds of the day. Upon examination of data, the settling tube appears to have operated routinely for the first 21 days of the deployment.

We display two key sets of data, again with the instrumentation point of view, leaving detailed scientific discussion to a later publication. The first is a history of optical transmission on 10 successive experimental days. In this case (Fig. 15) although due to different environmental conditions on different days, the initial optical transmission varies, the optical transmission increases in time, i.e. water monotonically clears as particles settle. Again, significantly, this observation is consistent with expectation, and, it contrasts with the earlier settling tube work of Zaneveld et al. (1982), and Hill et al. (1994). We interpret this monotonic increase in optical transmission to mean that there was no leakage into or out of the settling tube and that the initial turbulence was suppressed in a time-scale shorter than the shortest time at which any significant settling out occurs.

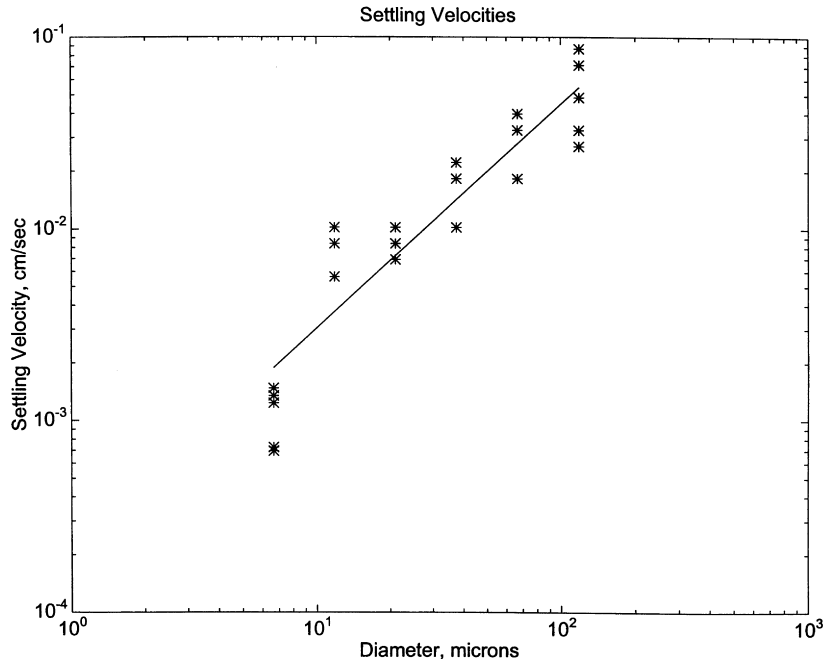


Fig. 17. Settling velocity estimates from a set of settling experiments at LEO-15.

Furthermore, the similarity of the transmission histories suggests that the particles were of a similar settling velocity distribution. This becomes evident when it is seen that the optical attenuation  $\tau$  is proportional to the sum of the concentration of the various component size classes. As each size class settles out, the transmission would then show an increase. Thus, a similar slope in the history on several days implies settling out of particles at near-equal times.

The concentration histories derived from the scattering are displayed in Fig. 16. The 8 size classes are identical for those of Fig. 11. In this case, we see a settling rate that is slower than the Stokes settling rate for siliceous particles in the smallest size classes, and an even greater divergence for the largest size classes. The fact that the particles in the smallest size classes settle out at all indicates that thermally driven residual motions are smaller than the smallest measurable settling velocity:  $30 \text{ cm}/8.6 \times 10^4 \text{ s}$ , or  $3.5 \times 10^{-4} \text{ cm/s}$ . In a separate paper, we shall publish the details of consistency between settling rate estimates obtained on different days. For now we note that the validity of Stokes settling for the lower Reynolds numbers, as verified in Fig. 11, permits us to estimate

the density of particles from their measured settling velocities. In Fig. 17, the settling velocity distribution is displayed for the particles at the LEO-15 site. Also displayed is a slope-2 line that would correspond to constant density particles falling in Stokes regime. The fact that the marine particles deviate from this behavior is an indication of the existence of floes. The departure from constant density line is more exaggerated at the larger sizes, suggesting that the larger particles are loose aggregates.

A simple fit to the data of Fig. 17 suggests a size vs. settling velocity relationship as:

$$w_f(d) = 0.45 \times 10^{-3} d^{1.17} \quad (11)$$

The generalized validity of this relation will be explored from the data at LEO-15 in a subsequent paper.

## 5. Discussion

The measurement of particle size distributions is of intrinsic interest to the marine scientist, whether from the point of view of sediment transport, biological

process studies or even bubble formation. The development of capabilities to estimate total suspended sediment concentration correctly, without errors introduced by changes in the natural particle size distribution is sure to add to the researchers' and the engineers' bag of tools. The autonomous capability of these devices permits long-term use for observations of episodic events, which in some places, do most of the transport of sediments.

The instrumentation described here does have limitations. For example, the consequence of the presence of very light aggregate type particles to the determination of size distribution is not known. The small-angle scattering properties of these marine aggregates need to be studied. Also, there is a strong body of literature suggesting, from photographs, that stringy scatterers are present in aquatic environments, (e.g. Honjo et al., 1984). Here, the sphere approximation is, of course, unsuitable. Diffraction theory predicts that thin cylinders produce streaked scattering in a plane normal to the plane containing the cylinder. Thus, strings produce streaks across the face of the ring-detector. If a streak lies on one quadrant of the detector, it produces a bias in that quadrant. This is frequently recognizable in the data as a sawtooth shape in the scattering signature. The same behavior has also been observed in the laboratory when scattering is observed from natural particles in still water. When turbulence is introduced, the scattering signature becomes smooth instantly. This effect is due to the establishment of preferred orientation of particles falling in still water. As these particles are also not spherical, the scattering has preferred orientations, again producing a sawtooth signature in the scattering data. These characteristics are helpful hints in learning more about the nature of the scatterers, although the quantification of such interpretation is as yet not possible.

A second limitation is in the range of turbidity that can be measured. We have observed that when the optical transmission is less than 30%, multiple-scattering effects begin to appear. This refers to the re-scattering of scattered light. The lower the transmission, the stronger the effects of multiple scattering. Theoretical investigations of multiple scattering reveal that if such effects are ignored, the recovered particle size distribution shows a bias toward the small sizes. Algorithms for multiple scattering are available

in the literature as applied to this problem (Hirleman, 1991).

When measuring settling velocities, there is a continual concern regarding the breakup of fragile aggregates in the process of drawing of a sample. There is no known way of estimating such floc damage at present. Perhaps an in-situ photographic approach can be used for an assessment.

### Acknowledgements

This paper is the result of several years of work supported first by Dr Joseph Kravitz of the Office of Naval Research under current contract no. N00014-95-C-0101, by Dr Curtis Olsen of the Department of Energy, contract no. DE-FG03-96-ER62179 and via a grant from NOAA under the NURP program managed by Dr Waldo Wakefield at Rutgers University. The authors acknowledge the many constructive comments of the reviewers who acquainted us with the work of Gibbs cited in the bibliography.

### Appendix A

The size distribution function  $n(a)$  is defined so that  $n(a)da$  represents the number of particles per unit volume of water, of size  $a$  in a size range  $da$ . Thus the area distribution is  $a^2n(a)$  and the volume distribution is given by  $a^3n(a)$ . We treat the measurement of optical attenuation, background scattering, both of which are necessary auxiliary measurements, and inversions below.

#### A.1. Optical attenuation

With reference to Fig. 1, let the laser output power be  $P_1$ . A fraction of this power  $(1 - \alpha)P_1$  is split off and sensed by the reference detector,  $P_r$ . The remaining,  $\alpha P_1$  enters water after some losses due to scattering off surfaces in the prism and pressure-resistant window. If  $\eta_{\text{trans}}$  is the overall optical efficiency of the components from the beam splitter till the laser beam enters water, then the laser power entering water will be  $= \alpha \eta_{\text{trans}} P_1$ . For the sake of simplicity, define  $P_0 = \alpha \eta_{\text{trans}} P_1$ . Consider first the case of pure filtered water. The power reaching the receiving window will be attenuated due to absorption in water. It is conven-

tional in ocean optics literature to use the symbol  $\mathbf{a}$  for pure water absorption (in  $\text{m}^{-1}$ ) so that the laser power reaching the receiving window will be  $e^{-\mathbf{a}l}P_0$ . Further optical losses due to reflections off optical surfaces can be included as another optical efficiency factor,  $\eta_{\text{recv}}$  so that the power sensed by the ‘transmissometer’ photodiode is  $e^{-\mathbf{a}l}P_0\eta_{\text{opt}2}$ . Combining the factors  $\alpha\eta_{\text{trans}}\eta_{\text{recv}}$  into an *overall optical efficiency*  $\eta_{\text{opt}} = \alpha\eta_{\text{trans}}\eta_{\text{recv}}$ , one sees that for the case of pure water, the ‘transmissometer’ diode sees a laser power given by

$$P_{\text{t,clear}} = e^{-\mathbf{a}l}\eta_{\text{opt}P_1} \quad (\text{A1})$$

The introduction of absorptive and/or scattering material, with an *additional* attenuation of light by absorption and scattering represented by  $c_A$  ( $\text{m}^{-1}$ ), will clearly change the power incident on the transmissometer photodiode to

$$P_{\text{t,turbid}} = \exp\{- (\mathbf{a} + c_A)l\}\eta_{\text{opt}P_1} \quad (\text{A2})$$

From the ratio of Eqs. A2 and A1, the transmissometer photodiode measures the *additional*  $c_A$  due to the dissolved and suspended material. When there is no dissolved absorbing material and the particles are non-absorbing,  $c_A = b$ , the total scattering, so that a direct measure of total scattering by particles is obtainable. In general, the measured attenuation will be the sum of that due to absorption and scattering by particles and due to any dissolved absorptive material. These quantities are of interest to optical oceanographers concerned with light propagation studies.

### A.2. Background light

The measurement of background light and its adequate subtraction from the total signal at the ring detector is important, especially when the scattering from particles is weak. Buchele (1988) has shown that if the background light is measured in the absence of scattering particles, then this background field should be first multiplied by  $\exp(-c_A l)$  before subtracting from the measurement which is the combined signal from particles and optical surfaces. This is incorporated in Eq. (5).

### A.3. Scattered light signal and inversion

For the geometry of Fig. 1, the optical power

scattered into a solid angle  $d\Omega$  from a single particle placed in the laser beam, at a distance  $x$  from the transmitting window is given by:

$$I = [P_0 e^{-cx}/A](i_1 + i_2) e^{-c(l-x)} d\Omega/k^2 \quad (\text{A3})$$

Where,  $i_1 + i_2$  are intensity functions defined in Van deHulst (1957) (p. 129), and where we explicitly show attenuation of the beam up to the particle as  $e^{-cx}$  and from the particle to the receiving window as  $e^{-c(l-x)}$ . It follows that an elementary volume, of diameter  $A$  and length  $dl$  with a particle number density  $n(a)da$  per unit volume would produce a scattering given by

$$I_1 = P_0 e^{-cl}(i_1 + i_2)dl n(a)da d\Omega/k^2 \quad (\text{A4})$$

In the above, the attenuation coefficient  $c$  is the sum of absorption by water, dissolved material, and particles, and attenuation by scattering by particles:

$$c = a_w + a_d + b \quad (\text{A5})$$

Now, the solid angle in the focal plane is:

$$d\Omega = \theta d\theta \quad (\text{A6})$$

so that, one writes for the power sensed by a single ring, after integrating along the optical path in water and after including the optical efficiency of the receiving optics:

$$E_i = \int \int \eta_{\text{recv}} P_0 e^{-cl}(i_1 + i_2)dl n(a)\theta da d\theta/k^2; \quad (\text{A7})$$

or

$$E_i = P_0 \eta_{\text{recv}} l e^{-cl}/k^2 \int n(a)a^2 da \int (i_1 + i_2)a^{-2} \theta d\theta$$

This equation, in a manner similar to Hirleman (1987), is rewritten in the discretized form:

$$\text{or } \bar{E} = [P_0 \eta_{\text{recv}} l e^{-cl}/k^2] \bar{\mathbf{K}} \bar{N}_A \quad (\text{A8})$$

Each element of the kernel matrix  $\bar{\mathbf{K}}$  is the inner integral, and each element of the vector  $\bar{N}_A$  is the area in the size range, as represented by the outer integral of Eq. (A7). The integrations are carried out, in angles and sizes, respectively, over  $\rho^{j-1}\theta_{\text{min}} < \theta < \rho^j\theta_{\text{min}}$  and  $\rho^{j-1}a_{\text{min}} < a < \rho^j a_{\text{min}}$ .

The photo-current from the corresponding ring is converted to a voltage using an operational amplifier circuit, and the voltage is digitized. If  $\mathbf{R}$  is the responsivity of the photo-diodes, and the gain (current-to-voltage) is  $G$ , then the voltage sensed will be  $G\mathbf{R}\bar{E}$ .

With a 12-bit 5 V full-scale A/D converter, the digital counts for the 32 rings will be given by the array  $\bar{d}$ :

$$\bar{d} = (4096/5)GR[P_0\eta_{\text{recvl}}e^{-cl}/k^2]\bar{\mathbf{K}}\bar{N}_A \quad (\text{A9})$$

This is the array noted in Eq. (5). The laser power  $P_0$  is simply a constant times the reference power  $P_r$ , the power sensed by the reference sensor (see Fig. 1). We now combine all the constants in front of the matrix product to write:

$$\bar{d} = K[P_r e^{-cl}]\bar{\mathbf{K}}\bar{N}_A \quad \text{or} \quad \bar{d} = K\tau P_r\bar{\mathbf{K}}\bar{N}_A \quad (\text{A10})$$

The measured digital counts include the scattering from background optical surfaces also, which is attenuated by  $\tau$  exactly as scattering is. Thus the measured digital counts are:

$$\bar{d} = K\tau P_r[\bar{\mathbf{K}}\bar{N}_A + \text{zscat}] \quad (\text{A11})$$

This is the basis for the formulation of Eq. (5). The constant  $K$  can be computed from above, or it can be estimated by calibrating a known particle size distribution as in Eq. (7).

#### A.4. Solution for $\bar{N}_A$

The inversion of Eq. (A3) is carried out using a modified Chahine method described by Riley and Agrawal (1991). This is a non-linear iterative solution and has been empirically determined to be the best performer. According to this method, the  $(n + 1)$ th iterate is computed from the  $n$ th by

$$N_{A,i}^{n+1} = N_{A,i}^n \xi \quad (\text{A12})$$

where  $\xi$  is the ratio of the measured scattering at the ring corresponding to size  $i$  and the magnitude of the predicted scattering at this ring from the previous iterate. Once a reasonable convergence is reached, the volume distribution is computed as (leaving out factors of  $\pi$ ):

$$V_{A,i} = 4/3a_i N_{A,i} \quad (\text{A13})$$

We have expressed this entire procedure in the shorthand INV(S) in Eq. (7). It should be noted that the mathematical problem of inversion continues to receive attention of researchers. A recent survey appears in a special issue of the journal *Applied Optics* (vol. 30, no. 33, 1991). The interested reader is encouraged to study the works of Twomey (1977)

and Hirleman (1987) which address the fundamental information content of data in inverse problems.

## References

- Agrawal, Y.C., Pottsmith, H.C., 1993. Optimizing the kernel for laser diffraction particle sizing. *Appl. Opt.* 32 (22), 4285–4286.
- Agrawal, Y.C., Pottsmith, H.C., 1994. Laser diffraction particle sizing in STRESS. *Continental Shelf Res.* 14 (10/11), 1101–1121.
- Agrawal, Y.C., Traykovski, P., 2000. Particles in the bottom boundary layer: concentration and size dynamics through events. *J. Geophys. Res.* (in press).
- Bale, A.J., Morris, A.W., 1987. In situ measurement of particle size in estuarine waters. *Estuarine Coastal Shelf Sci.* 24, 253–263.
- Born, M., Wolf, E., 1975. *Principles of Optics*, Pergamon, New York, p. 808.
- Buchele, D.R., 1988. Particle sizing by weighted measurements of scattered light, NASA-TM-100968, NASS.
- Crawford, P., Hay, A.E., 1993. Determining suspended sand size and concentration from multi-frequency acoustic backscatter. *J. Acoustic Soc. Am.* 94, 3312–3324.
- Dietrich, W.E., 1982. Settling velocity of natural particles. *Water Resour. Res.* 18 (6), 1615–1626.
- Downing, J.P., Sternberg, R.W., Lister, C.R.B., 1981. New instrumentation for the investigation of sediment suspension processes in the shallow marine environment. *Mar. Geol.* 42, 19–34.
- Dyer, K.R., et al., 1996. A Comparison of in-situ techniques for estuarine floc settling velocity measurements. *J. Sea Res.* 36 (1/2), 15–29.
- Eisma, D., et al., 1996. Intercomparison of in-situ suspended matter (floc) size measurements. *J. Sea Res.* 36 (1/2), 3–14.
- Fennessy, M.J., Dyer, K.R., Huntley, D.A., 1994. INSSEV: an instrument to measure the size and settling velocity of flocs in-situ. *Mar. Geol.* 117, 107–117.
- Gentien, P., Lunven, M., Lehaitre, M., Duvent, J.L., 1995. In-situ depth profiling of particle sizes. *Deep-Sea Res.* 42 (8), 1297–1312.
- Gibbs, R.J., 1982. Floc breakage during HIAC light-blocking analysis. *Environ. Sci. Technol.* 16 (5), 298–299.
- Gibbs, R.J., Konwar, L.N., 1982. Effect of pipetting on mineral flocs. *Environ. Sci. Technol.* 16 (2), 119–121.
- Gibbs, R.J., Konwar, L.N., 1983. Sampling of mineral flocs using Niskin bottles. *Environ. Sci. Technol.* 17 (6), 374–375.
- Hay, A.E., Sheng, J., 1992. Vertical profiles of suspended sand concentration and size from multifrequency acoustic backscatter. *J. Geophys. Res.* 97 (C10), 15 661–15 677.
- Hill, P.S., Sherwood, C.R., Sternberg, R.W., Nowell, A.R.M., 1994. In situ measurements of particle settling velocity on the northern California continental shelf. *Continental Shelf Res.* 14 (10/11), 1123–1138.
- Hirleman, E.D., 1987. Optimal scaling of the inverse Fraunhofer diffraction particle sizing problem: the linear system produced by quadrature. *Particle Characterization* 4, 128–133.

- Hirleman, E.D., 1991. General solution to the inverse near-forward-scattering particle-sizing problem in multiple-scattering environments: theory. *Appl. Opt.* 30 (33), 4832–4838.
- Honjo, S., Doherty, K.W., Agrawal, Y.C., Asper, V.L., 1984. Direct optical assessment of large amorphous aggregates (marine snow) in the deep ocean. *Deep-Sea Res.* 31 (1), 67–76.
- Jones, S.E., Jago, C.F., 1996. Determination of settling velocity in the Elbe estuary using quisset tubes. *J. Sea Res.* 36 (1/2), 63–67.
- Lynch, J.F., Irish, J.D., Sherwood, C.R., Agrawal, Y.C., 1994. Determining suspended sediment particle size information from acoustical and optical backscatter measurements. *Continental Shelf Res.* 14 (10/11), 1139–1165.
- Moody, J.A., Butman, B., Bothner, M.H., 1987. Near-bottom suspended matter concentration on the continental shelf during storms: estimates based on in-situ observations of light transmission and a particle size dependent transmissometer calibration. *Continental Shelf Res.* 7 (6), 609–628.
- Puls, W., Kuhl, H., 1996. Settling velocity determination using the Bigdan settling tube and the Owen settling tube. *J. Sea Res.* 36 (1/2), 119–125.
- Riley, J.B., Agrawal, Y.C., 1991. Sampling and inversion of data in diffraction particle sizing. *Appl. Opt.* 30 (33), 4800–4817.
- Rouse, H., 1937. Modern conceptions of the mechanics of fluid turbulence. *Trans. Am. Soc. Civil Engng* 102, 463–554.
- Smith, J.D., 1977. *Modeling of Sediment Transport on Continental Shelves, the Sea*, Wiley, New York, pp. 539–577.
- Swithenbank, J., Beer, J.m., Taylor, D.S., Abbot, D., McCreath, G.C., 1976. A laser diagnostic technique for the measurement of droplet and particle size distribution, AIAA, New York, pp. 76–79.
- Thorne, P.D., Hardcastle, P., 1997. Acoustic measurements of suspended sediments in turbulent currents and comparison with in-situ sampling. *J. Acoustic Soc. Am.* 101, 2603–2614.
- Traykovski, P., Latter, R., Irish, J.D., 1999. A laboratory evaluation of the laser in-situ scattering and transmissometry instrument using natural sediments. *Mar. Geol.* 159, 355–367.
- Twomey, S., 1977. *An Introduction to the Mathematics of Inversion. Remote Sensing and Indirect Measurements*, Elsevier, Amsterdam, p. 243.
- Van Leussen, W., 1996. The RWS field settling tube. *J. Sea Res.* 36 (1/2), 83–86.
- Van deHulst, H., 1957. *Light Scattering by Small Particles*, Dover, New York, p. 470.
- Wiberg, P.L., 1995. A theoretical investigation of boundary layer flow and bottom shear stress for smooth, transitional, and rough flow under waves. *J. Geophys. Res.* 100 (C11), 22 667–22 679.
- Yariv, A., 1988. *Optical Electronics*, Holt, Rinehart, and Winston, New York, p. 551.
- Zaneveld, J.R.V., Sprinrad, R.W., Bartz, R., 1982. An optical settling tube for the determination of particle size distribution. *Mar. Geol.* 49, 357–376.